PHYSICAL REVIEW E **75**, 056314 (2007)

Interfacial dynamics in pressure-driven two-layer laminar channel flow with high viscosity ratios

O. K. Matar and C. J. Lawrence
Department of Chemical Engineering, Imperial College London, South Kensington Campus, London, SW7 2AZ, United Kingdom

G. M. Sisoev
School of Mathematics, University of Birmingham, Edgbaston, Birmingham, B15 2TT, United Kingdom

(Received 28 November 2006; published 30 May 2007)

The large-scale dynamics of an interface separating two immiscible fluids in a channel is studied in the case of large viscosity contrasts. A long-wave analysis in conjunction with the Kármán-Polhausen method to approximate the velocity profile in the less viscous fluid is used to derive a single equation for the interface. This equation accounts for the presence of interfacial stress, capillarity, and viscous retardation as well as inertia in the less viscous fluid layer where the flow is considered to be quasistatic; the equation is shown to reduce to a Benney-type equation and the Kuramoto-Sivashinskiy equation in the relevant limits. The solutions of this equation are parametrized by an initial thickness ratio h_0 and a dimensionless parameter $\mathcal{S}$, which measures the relative significance of inertial to capillary forces. A parametric continuation technique is employed, which reveals that nonuniqueness of periodic solutions is possible in certain regions of $(h_0, \mathcal{S})$ space. Transient numerical simulations are also reported, whose results demonstrate good agreement with the bifurcation structure obtained from the parametric continuation results.

DOI: 10.1103/PhysRevE.75.056314 PACS number(s): 47.55.N−

I. INTRODUCTION

Thin liquid films are of central importance in many engineering, daily-life, biomedical, geophysical, and microgravity settings and applications. Not surprisingly, their dynamics have received considerable attention with many modeling and experimental papers appearing in the literature over the past several decades in connection with heat and mass transfer in distillation units, heat exchangers, falling film reactors, coating flow technologies, adhesives, foams, surfactant replacement therapy, tear-film rupture, gravity currents, and lava, oil, and gas flows in wells and pipelines, cooling of nuclear installations, microfluidic, and microelectromechanical devices [1–14].

Studies involving two phases have focused on gas-liquid flows due to their obvious relevance to the oil and gas industry and to the design and operation of pipelines and process equipment. Previous work in this area has attempted to predict changes in the flow regimes in gas-liquid flows in pipelines and channels with particular emphasis on the transition from stratified to slug flow [15–17]. A variety of methods have been used, ranging from linear stability analyses using the long-wave approximation [16,18] and Orr-Sommerfeld calculations [19–25] (for both bounded and unbounded two-layer flows) to one-dimensional, averaged equations (for the liquid-phase volume fraction, gas density, and gas and liquid velocities; see, for instance, [26,27] and references therein) and direct numerical simulations of mixing layers and core-annular flows [28–31]. Multilayers of stratified films have also been studied mainly in connection with geophysical flows and industrial applications such as the coating of photographic films and papers (see, for instance, [32,33] and references therein) but these studies have focused mainly on flows with an upper free surface.

The important work of Tilley *et al.* [34,35] in this area deserves particular attention. These authors derived a strongly nonlinear evolution equation for the interface separating two viscous, immiscible layers in an inclined channel using long-wave theory [34]. This involved the use of a regular perturbation expansion in powers of the wave number, assumed to be small, which gave rise to an equation that accounts for viscosity and density stratification, interfacial shear, and capillarity, as well as inertial forces. These authors then derive a generalized version of the Kuramoto-Sivashinskiy (KS) equation and, in the limit wherein the coefficient of the advection term is very small, they derive a modified version of the KS equation, with a cubic nonlinearity in addition to the usual quadratic advection term; this nonlinearity reflects the contribution of the two-phase nature of the flow. They then demonstrate through weakly nonlinear and bifurcation analyses how the inclusion of this cubic term alters the properties of the KS equation. For instance, Tilley *et al.* [34] showed that steady-state solutions of the KS equation become traveling waves in the modified KS equation and, for sufficiently strong cubic nonlinearities, jumps occurred from small to "large"-amplitude traveling-wave solutions, which were interpreted as a precursor to the so-called "flooding" phenomenon in gas-liquid flows; this hysteretic behavior is also absent in the KS system. Analogous behavior was also observed by Papageorgiou *et al.* [36] in their study of the stability of core-annular flows, which demonstrated the existence of traveling-wave solutions in their modified KS equation (which included a nonlinear integral term) in parameter ranges wherein chaotic solutions of the KS equation were determined.

Tilley *et al.* [35] also analyzed the long-wave and full linear stability characteristics of the two-layer system. Their results for an air-water system in horizontal channels demonstrate the existence of short- and long-wavelength traveling waves, while for horizontal oil-water systems they show that the primary instability mode could be odd; this has no analog in single-phase pressure-driven flows. In inclined channels, their results indicate that in air-water systems, the interface is unstable to long-wave disturbances, while for oil-water systems the possibility of a co-dimension two point was demonstrated reflecting the competition between odd shear and interfacial modes. The recent work by Segin *et al.* [37,38] considered the flow of two immiscible fluids in an inclined channel and used lubrication theory to derive evolution equations for the interface shape and pressure; here, the ratio of the channel height to the disturbance wavelength constitutes the small parameter. These authors focused on situations relevant to countercurrent air-water systems and considered different constraints on the flow: either a constant air flow rate or a fixed water flow rate and pressure drop. Their numerical simulations demonstrate the presence of lax and undercompressive shocks as well as rarefaction waves depending on system parameters, and these results are of relevance to flooding in gas-liquid flows.

In spite of the large number of studies devoted to two-layer flows, few studies have examined the behavior of the interface separating two viscous, immiscible fluids constrained to flow in a channel in the strongly nonlinear regime. In this paper, we consider the problem of a two-layer flow in a channel in which a layer of a relatively fast-flowing fluid flows past a film of a much more viscous fluid. We use long-wave theory and the Kármán-Polhausen (KP) approximation to derive a single, nonlinear evolution equation that governs the interfacial dynamics; a parabolic velocity profile is used for the fast-flowing layer in which the flow is assumed to be in the laminar regime. The resulting equation accounts for the presence of inertia, interfacial stress, capillarity, and viscous dissipation. Here, we consider fluids of similar densities so that the results of this work are more relevant to cleaning-type applications (wherein a highly viscous fluid is washed away by a fast-flowing water layer, for instance), thereby distinguishing this work from previous studies which have focused on gas-liquid flows. We show how, for sufficiently small mean film thicknesses, these equations can be reduced to Benney-like equations [39] and the well-studied KS equation. We focus, however, on elucidating the behavior of the system in the strongly nonlinear regime for a film thickness range which renders both the Benney and KS equations invalid. Our numerical investigation using bifurcation theory and transient numerical simulations reveals the development of interfacial waves during the flow; good agreement is achieved between the results of the simulations and those of the bifurcation analysis.

The rest of this paper is organized as follows. In Sec. II, we present the derivation of the evolution equations. In Secs. III and IV, we present the results of our bifurcation analysis and transient numerical simulations. Finally, concluding remarks are provided in Sec. V.

II. PROBLEM FORMULATION

A. Governing equations

We consider the flow of a layer of incompressible fluid of constant viscosity μ_w and density ρ_w past a thin film of viscous fluid which has dynamic viscosity μ and the same density $\rho=\rho_w$. The flow takes place in a horizontal channel of height H. We use a rectangular coordinate system (x,z) to model the dynamics, in which x and z correspond to the horizontal and vertical directions, respectively. The fluids of viscosity μ_w and μ are located in $h\leqslant z\leqslant H$ and $0\leqslant z\leqslant h$, respectively, where $z=h(x,t)$ represents the location of the interface; these will be referred to henceforth as the "upper" and "lower" fluids, respectively, despite the fact that gravitational effects are neglected.

In the upper layer, we have the following equations of mass and momentum conservation:

$$U_x+W_z=0, \tag{1}$$

$$\rho_w(U_t+UU_x+WU_z)=-P_x+\mu_w(U_{xx}+U_{zz}), \tag{2}$$

$$\rho_w(W_t+UW_x+WW_z)=-P_z+\mu_w(W_{xx}+W_{zz}). \tag{3}$$

Here, U, W, and P represent the horizontal and vertical components of the velocity field and pressure in the upper layer, respectively; t denotes time. (The uppercase symbols are used to designate variables associated with the upper layer.)

In the lower layer, we have

$$u_x+w_z=0, \tag{4}$$

$$\rho(u_t+uu_x+wu_z)=-p_x+\mu(u_{xx}+u_{zz}), \tag{5}$$

$$\rho(w_t+uw_x+ww_z)=-p_z+\mu(w_{xx}+w_{zz}). \tag{6}$$

Here, u, w, and p represent the horizontal and vertical components of the velocity field and pressure in the lower layer, respectively.

At the interface, $z=h(x,t)$, we demand continuity of the stress and velocity components, in addition to the kinematic boundary condition:

$$P-p-2\mu_w\frac{(W_z-h_xU_z+U_xh_x^2-h_xW_x)}{1+h_x^2}+2\mu\frac{w_z-h_xu_z+u_xh_x^2-h_xw_x}{1+h_x^2}=\sigma\frac{h_{xx}}{(1+h_x^2)^{3/2}}, \tag{7}$$

$$\mu_w[(U_z+W_x)(1-h_x^2)+2h_x(W_z-U_x)]=\mu[(u_z+w_x)(1-h_x^2)+2h_x(w_z-u_x)], \tag{8}$$

$$h_t+uh_x=w, \tag{9}$$

$$u=U, \quad w=W. \tag{10}$$

Here, σ denotes surface tension, taken to be constant. At the channel walls $z=0$ and $z=H$, we demand no slip and no penetration:

$$u=w=0, \quad U=W=0. \tag{11}$$

B. Scaling

In order to render the above equations and boundary conditions dimensionless we adopt the scalings

$$x=\mathcal{L}\tilde{x},\quad (z,h)=H(\tilde{z},\tilde{h}),\quad t=(\mathcal{L}/V)\tilde{t},$$

$$(u,U)=V(\tilde{u},\tilde{U}),\quad (w,W)=\epsilon V(\tilde{w},\tilde{W}),\quad p=\left(\frac{\mu_w V\mathcal{L}}{H^2}\right)\tilde{p}. \tag{12}$$

Here, V is the superficial velocity of the upper layer assumed to be constant and $\epsilon=H/\mathcal{L}\ll 1$, in which $\mathcal{L}$ is a length scale to be defined below. Substitution of these scalings into the governing equations and boundary conditions yields the following dimensionless mass and momentum conservation equations:

$$U_x+W_z=0, \tag{13}$$

$$\epsilon\,\mathrm{Re}(U_t+UU_x+WU_z)=-P_x+U_{zz}+\epsilon^2 U_{xx}, \tag{14}$$

$$\epsilon\,\mathrm{Re}(W_t+UW_x+WW_z)=-\frac{1}{\epsilon^2}P_z+W_{zz}+\epsilon^2 W_{xx}, \tag{15}$$

$$u_x+w_z=0, \tag{16}$$

$$\epsilon m\,\mathrm{Re}(u_t+uu_x+wu_z)=-mp_x+u_{zz}+\epsilon^2 u_{xx}, \tag{17}$$

$$\epsilon m\,\mathrm{Re}(w_t+uw_x+ww_z)=-\frac{m}{\epsilon^2}p_z+w_{zz}+\epsilon^2 w_{xx}. \tag{18}$$

Here, $m\equiv\mu_w/\mu$ and $\mathrm{Re}\equiv\rho_w VH/\mu_w$ is a Reynolds number, reflecting the relative significance of inertial to viscous forces in the upper layer. The dimensionless interfacial stress boundary conditions are expressed by

$$\begin{aligned}P-p&-\frac{2\epsilon^2}{(1+\epsilon^2h_x^2)}(W_z-h_xU_z+\epsilon^2h_x[h_xU_x-W_x])\\&+\frac{2\epsilon^2}{m(1+\epsilon^2h_x^2)}(w_z-h_xu_z+\epsilon^2h_x[h_xu_x-w_x])\\&=\frac{\epsilon^3}{\mathrm{Ca}}\frac{h_{xx}}{(1+\epsilon^2h_x^2)^{3/2}},\end{aligned} \tag{19}$$

$$\begin{aligned}m[(U_z+\epsilon^2W_x)(1-\epsilon^2h_x^2)+2\epsilon^2h_x(W_z-U_x)]\\=[(u_z+\epsilon^2w_x)(1-\epsilon^2h_x^2)+2\epsilon^2h_x(w_z-u_x)],\end{aligned} \tag{20}$$

where $\mathrm{Ca}\equiv\mu V/\sigma$ is a capillary number and the rest of the conditions remain unchanged.

C. Asymptotic reduction and the integral method

We promote inertia in the upper layer by considering the distinguished limit $\mathrm{Re}\sim\epsilon^{-1}$ and $\mathrm{Ca}\sim\epsilon^3$ and by performing the rescalings

$$\mathrm{Re}=\frac{\tilde{\mathrm{Re}}}{\epsilon},\quad \mathrm{Ca}=\epsilon^3\tilde{\mathrm{Ca}},\quad (u,w)=m(\tilde{u},\tilde{w}),\quad t=\frac{\tilde{t}}{m}; \tag{21}$$

we also choose $\mathcal{L}\equiv H/m$ so that $\epsilon=m$. Here, the upper and lower layers are governed by the steady boundary layer equations and lubrication theory, respectively. The resulting leading-order equations are given by

$$U_x+W_z=0, \tag{22}$$

$$\tilde{\mathrm{Re}}(UU_x+WU_z)=-P_x+U_{zz}+O(\epsilon^{1/2}), \tag{23}$$

$$P_z=0+O(\epsilon^2), \tag{24}$$

$$\tilde{u}_x+\tilde{w}_z=0, \tag{25}$$

$$p_x=\tilde{u}_{zz}+O(\epsilon), \tag{26}$$

$$p_z=0+O(\epsilon^2), \tag{27}$$

$$P=p+\frac{h_{xx}}{\tilde{\mathrm{Ca}}}+O(\epsilon^2),\quad U_z=\tilde{u}_z\equiv\tau_i+O(\epsilon^{1/2}),\quad \text{at } z=h, \tag{28}$$

$$h_{\tilde{t}}+\tilde{u}h_x=\tilde{w}+O(\epsilon^{3/2}),\quad U=W=0+O(\epsilon^{1/2}),\quad \text{at } z=h, \tag{29}$$

$$\tilde{u}=\tilde{w}=0,\quad \text{at } z=0, \tag{30}$$

$$U=W=0,\quad \text{at } z=1, \tag{31}$$

where τ_i denotes interfacial stress.

In the lower layer, we obtain the following expression for $\tilde{u}$ via integration of Eq. (26) and application of the shear stress and no-slip conditions at $z=h$ and $z=0$ given by Eqs. (28) and (30), respectively:

$$\tilde{u}=z\tau_i+\frac{1}{2}(z^2-2zh)p_x. \tag{32}$$

Combination of Eqs. (25) and (30) and the kinematic boundary condition yields the following evolution equation for h:

$$h_{\tilde{t}}+\left(\frac{1}{2}h^2\tau_i-\frac{1}{3}h^3p_x\right)_x=0. \tag{33}$$

In the upper layer, we use an integral method. First, we integrate Eqs. (22) and (23) from $z=h$ to $z=1$ to get

$$Q_x=0+O(\epsilon^{1/2}), \tag{34}$$

$$\tilde{\mathrm{Re}}\left(\int_h^1 U^2dz\right)_x+(1-h)P_x+\tau_w+\tau_i=0+O(\epsilon^{1/2}), \tag{35}$$

where $\tau_w\equiv-\tilde{U}_z|_{z=1}$ is the wall shear stress in the upper phase and we have made use of the interfacial boundary conditions. Equation (34) indicates that $Q\equiv Q_0=1$.

We then adopt the following form for U, which satisfies the boundary conditions at $z=h$ and $z=1$:

$$U=\frac{-6}{(1-h)^3}[z^2-(1+h)z+h]. \tag{36}$$

Substitution of this equation into Eq. (35) yields the following expression for the pressure gradient in the upper phase:

$$P_x = -\frac{6}{5(1-h)^3}(10 + \widetilde{\mathrm{Re}}\, h_x). \tag{37}$$

Since $p_x = P_x - h_{xxx}/\widetilde{\mathrm{Ca}}$ and $\tau_i = 6/(1-h)^2$, we obtain from Eq. (33) the following evolution equation for h:

$$h_{\tilde{t}} + \left(\frac{2\,\widetilde{\mathrm{Re}}}{5(1-h)^3}h^3 h_x + \frac{h^2(3+h)}{(1-h)^3} + \frac{1}{3\widetilde{\mathrm{Ca}}}h^3 h_{xxx}\right)_x = 0. \tag{38}$$

It is possible to introduce the rescalings $x = (3\widetilde{\mathrm{Ca}})^{-1/3}\hat{x}$ and $\tilde{t} = (3\widetilde{\mathrm{Ca}})^{-1/3}\hat{t}$ to finally obtain (following suppression of the caret)

$$h_t + \left(\frac{\mathcal{S}}{(1-h)^3}h^3 h_x + \frac{h^2(3+h)}{(1-h)^3} + h^3 h_{xxx}\right)_x = 0, \tag{39}$$

where $\mathcal{S} \equiv \frac{2}{5}\widetilde{\mathrm{Re}}(3\widetilde{\mathrm{Ca}})^{1/3}$. The terms in the brackets correspond to inertia, shear, and capillarity, respectively.

We also derive an evolution equation for h using the so-called "method of weighted residuals" approach in which the test function, Eq. (36), is used in conjunction with

$$\phi = \frac{-6}{(1-h)}[z^2 - (1+h)z + h] \tag{40}$$

as the weighting function [40–44]. This approach yields an equation which is almost identical to Eq. (39) with the corresponding parameter $\mathcal{S}' \equiv \frac{18}{35}\widetilde{\mathrm{Re}}(3\widetilde{\mathrm{Ca}})^{1/3} = \frac{9}{7}\mathcal{S}$.

D. Limiting cases

Here we show that Eq. (39) can be related to other, well-studied, thin-film evolution equations. In the limit $h \ll 1$, we keep terms within $O(h^4)$ and Eq. (39) reduces to

$$h_t + \left[\mathcal{S}h^3 h_x + 3h^2\left(1 + \frac{10}{3}h + 7h^2\right) + h^3 h_{xxx}\right]_x = 0. \tag{41}$$

It is then possible to remove the parameter $\mathcal{S}$ by introducing the rescalings

$$x = \frac{\hat{x}}{\sqrt{\mathcal{S}}}, \quad t = \frac{\mathcal{S}^{1/4}}{3^{3/2}}\hat{t}, \quad h = \frac{\sqrt{3}}{\mathcal{S}^{3/4}}\hat{h} \tag{42}$$

into Eq. (41) to give (following suppression of the caret):

$$h_t + \left[h^3 h_x + h^2\left(1 + \frac{10}{\sqrt{3}\mathcal{S}^{3/4}}h + \frac{21}{\mathcal{S}^{3/2}}h^2\right) + h^3 h_{xxx}\right]_x = 0. \tag{43}$$

For large values of $\mathcal{S}$ we get from Eq. (43)

$$h_t + (h^3 h_x + h^2 + h^3 h_{xxx})_x = 0, \tag{44}$$

which is an evolution equation that is expected to exhibit "Benney-like" behavior, although it is not anticipated that finite-time blowup will occur since the nonlinearity of the inertial term $h^3 h_x$ in this case is weaker than that of the corresponding term in the Benney equation, $h^6 h_x$, and is comparable to that arising in the stabilizing capillary term.

We seek small-amplitude nonlinear wave solutions of this equation by writing

$$h = \epsilon(1 + \epsilon^2\tilde{h}), \quad \tau = \epsilon^3 t, \quad \xi = x - 2\epsilon t, \quad \epsilon \ll 1, \tag{45}$$

where $\tilde{h}(\xi,\tau)$ and τ is a time variable (which should not be confused with the shear stress which also has the symbol τ). Substitution of Eq. (45) into Eq. (44) yields, within up $O(\epsilon^6)$, the celebrated Kuramoto-Sivashinskiy equation [45–47] (following the suppression of the wave decoration)

$$h_\tau + (h^2)_\xi + h_{\xi\xi} + h_{\xi\xi\xi\xi} = 0. \tag{46}$$

The results are presented next.

III. STEADY REGULAR WAVES

In this section, we use bifurcation theory to demonstrate that Eq. (39) admits steady perodic waves, which are referred to below as "regular" waves. We begin, however, with a brief assessment of the linear stability properties of Eq. (39).

A. Linear stability analysis

A linear stability analysis of Eq. (39) is carried out using normal modes:

$$h(x,t) = h_0 + \hat{h}\exp i(kx - \omega t), \tag{47}$$

where $\hat{h}$ denotes the amplitude of a linear perturbation to the uniform base state, h_0, which has a (real) wave number k and a (complex) growth rate ω. Substitution of this decomposition into Eq. (39) and linearizing yields the equation

$$\omega = \frac{6h_0(1+h_0)}{(1-h_0)^4}k + ik^2 h_0^3\left(\frac{\mathcal{S}}{(1-h_0)^3} - k^2\right). \tag{48}$$

The imaginary part of the growth rate, $\mathrm{Im}(\omega) = \omega_i$ determines whether applied perturbations grow or decay. Thus $\omega_i > 0$ for $0 \leqslant k \leqslant k_c$, where $k_c = [\mathcal{S}/(1-h_0)^3]^{1/2}$ denotes the wave number of the cutoff mode, indicating the presence of a linear instability driven by inertia and mitigated by capillarity. The growth rate of the "most dangerous" mode, which has wave number $k_m = k_c/\sqrt{2} = [\mathcal{S}/2(1-h_0)^3]^{1/2}$, is $\omega_m = h_0^3\mathcal{S}/2(1-h_0)^3$. These results also indicate that for $h_0 \ll 1$, $(k_c, k_m) \sim \mathcal{S}^{1/2}$ and $\omega_m \sim h_0^3\mathcal{S}$ and the wavelength of unstable perturbations decreases as $(1-h_0)^{3/2}$ as $h_0 \to 1$, as shown in Fig. 1; it is expected that the present long-wave theory would break down in the latter limit.

B. Nonlinear waves

In order to determine time-periodic solutions of Eq. (39), we introduce the variables

$$\tau = \omega t, \quad \xi = \omega x, \quad \omega = \frac{2\pi}{T},$$

where T is the wave period. As a result, Eq. (39) is rewritten as

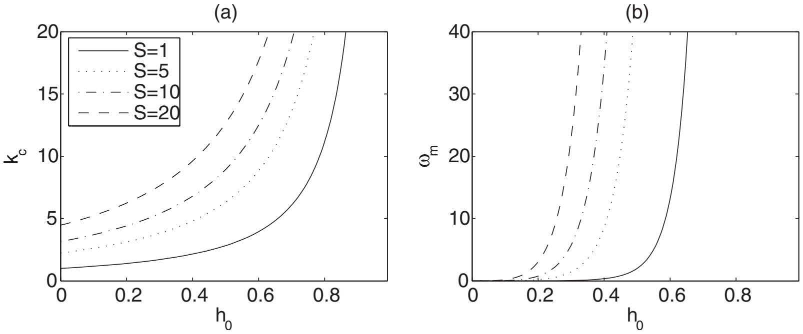

FIG. 1. Neutral stability curves: the variation of k_c and ω_m with h_0 is plotted for several values of the parameter $\mathcal{S}$ in (a) and (b), respectively.

$$\frac{\partial h}{\partial \tau}+\frac{\partial}{\partial \xi}\left[\frac{\mathcal{S}\omega}{(1-h)^3}h^3\frac{\partial h}{\partial \xi}+\frac{h^2(3+h)}{(1-h)^3}+\omega^3h^3\frac{\partial^3 h}{\partial \xi^3}\right]=0, \tag{49}$$

and it is convenient to use the normalized frequency s:

$$s=\frac{\omega}{\omega_c},\quad \omega_c=\beta\sqrt{\mathcal{S}},\quad \beta=\frac{6h_0(1+h_0)}{(1-h_0)^{11/2}},$$

where ω_c is the neutral wave frequency. We then seek solutions of the form $h(\eta)$ where $\eta=\alpha\xi-\tau$ and α is an unknown wave number. Substitution of this solution into Eq. (49) and subsequent integration lead to

$$-h+\alpha\left[\frac{\alpha\beta S^{3/2}s}{(1-h)^3}h^3\frac{dh}{d\eta}+\frac{h^2(3+h)}{(1-h)^3}+\alpha^3\beta^3S^{3/2}s^3h^3\frac{d^3h}{d\eta^3}\right]=A, \tag{50}$$

where A is a constant.

For time-periodic solutions Eq. (49) leads to

where $q_m^{(1)}$ is a constant flow rate calculated from the waveless flow:

$$q^{(1)}=2\pi\frac{H_0^2(3+h_0)}{(1-h_0)^3}.$$

Integration of Eq. (50) and making use of Eq. (51) allows the determination of the constant A, which is given by

$$A=\frac{1}{2\pi}\left(-\int_{\eta-2\pi}^{\eta}h\,d\eta+\alpha q^{(1)}\right). \tag{52}$$

Equation (50) may be rewritten as

$$\alpha^4\beta^3S^{3/2}s^3h^3(1-h)^3\frac{d^3h}{d\eta^3}+\alpha^2\beta S^{3/2}sh^3\frac{dh}{d\eta}+\alpha h^2(3+h)-(1-h)^3(A+h)=0. \tag{53}$$

Solutions of this equation are obtained subject to Eq. (52) and the periodic boundary conditions

$$h|_{\eta}=h|_{\eta+2\pi},\quad \left.\frac{dh}{d\eta}\right|_{\eta}=\left.\frac{dh}{d\eta}\right|_{\eta+2\pi}, \tag{54}$$

$$\left.\frac{d^2h}{d\eta^2}\right|_{\eta}=\left.\frac{d^2h}{d\eta^2}\right|_{\eta+2\pi}$$

and are invariant under the transformation $\eta\to\eta+\Delta\eta$.

Equations (52)–(54) are discretized using a pseudospectral method with the resulting nonlinear algebraic system solved using a Newton-Kantorovich method [48,49]; examples of steady-traveling waves are shown in Fig. 2. It is clearly seen that the waves have solitarylike shapes at small wave numbers which give way to more sinusoidal-shaped waves as the wave number tends to the neutral normalized wave number $s=1$. It is possible to transform any of the waves shown in Fig. 2 into another via continuous variation of the governing parameter s (or ω). The variation of the maximal film thickness h_{max} with the normalized wave number s was also investigated for different values of h_0. These "families" of solutions represent the so-called "dominating-wave" solutions (no other wave families are shown in Fig. 3 for a given s, $\mathcal{S}$, and h_0), a concept introduced in order to circumvent problems associated with solution nonuniqueness, which is evident in the equations that describe falling film flow as demonstrated by the work of Sisoev and Shkadov [50,51]; this feature complicates comparisons between modeling predictions and experimental observations. These authors have shown that in spite of solution nonuniqueness, which occurs in the computation of traveling waves via solution of the nonlinear eigenvalue problem, only the "dominating waves″ correspond to attracting solutions of the evolution equations; these attracting solutions are also the ones most likely to be observed experimentally. One would therefore expect that the numerical solution of Eq. (39) would correspond to the traveling-wave solutions of Eqs. (52)–(54) of maximal thickness, for a given s, $\mathcal{S}$, and h_0. As shown in Fig. 3, only one dominating-wave solution exists at any given value of s for relatively small values of h_0. For values larger than approximately $h_0=0.4$ (with $\mathcal{S}=10$), however, even the wave families corresponding to the dominating waves exhibit solution nonuniqueness; similar behavior was also observed by Sisoev and Shkadov [50] in their work on falling films. This nonuniqueness is reflected by the sudden jumps in the solution amplitude for fixed s; for sufficiently large h_0, h_{max} approaches unity and these results should be interpreted with caution since they were generated for parameter values that may render the long-wave assumption invalid. Nevertheless, this hysteretic behavior is reminiscent of that observed by Tilley *et al.* [34] for sufficiently strong cubic nonlinearities in their modified KS equation and was considered by these authors as being a precursor to "flooding." In the next section, we show through the results of transient computations of Eq. (39) that the waves depicted in Figs. 2 and 3 correspond to dominating waves and that solu-

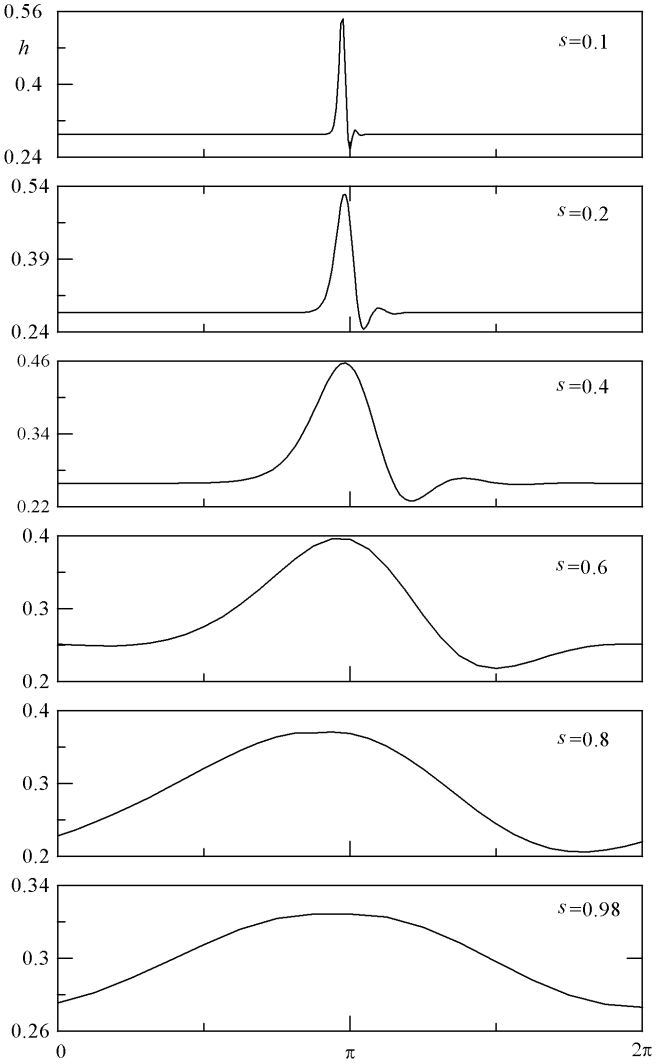

FIG. 2. Steady-traveling waves generated via solution of Eqs. (52)–(54) for different normalized frequencies s, with $\mathcal{S}=10$ and $h_0=0.3$.

tions in the h_0 range where hysteresis was observed in Fig. 3 culminate in channel-bridging events.

IV. TRANSIENT NUMERICAL SIMULATIONS

Here we present the results of a parametric study of Eq. (39) via transient numerical simulations. Results are presented for "natural" and "forced" waves; the latter are obtained via inlet forcing of the film with a prescribed frequency and amplitude, while the former are determined in the absence of such forcing. The forced-wave results are compared with the regular waves obtained in the previous section for the same values of the wave frequency, $\mathcal{S}$ and h_0. We begin, however, with a brief description of the numerical procedure used to carry out the simulations.

A. Numerical procedure

Some of the computations were carried out using EPDCOL [52], which uses finite-element collocation for the discretization of spatial derivatives and Gear's method in time. This routine was previously used to provide accurate solutions of related thin-film problems [53–56]. Additional computations were performed using a numerical procedure which employed centered differences in space and Gear's method in time. This procedure exploited the sparsity of the matrices generated as a result of spatial discretization which enhanced the efficiency of the computations substantially. Both EPDCOL and the finite-difference procedure were used to simulate the formation of natural and forced waves.

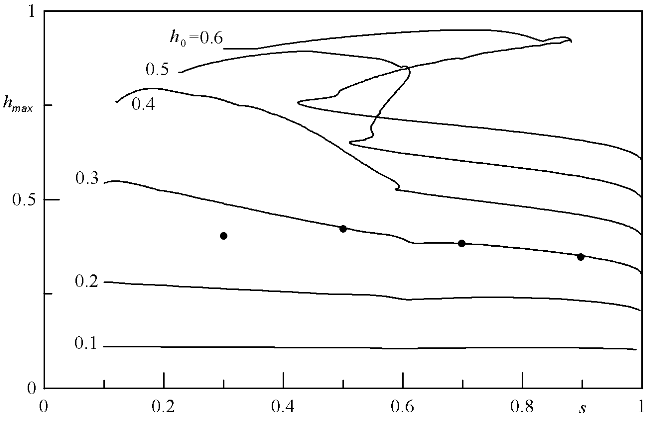

FIG. 3. The variation of the maximal wave thicknesses h_{max}, with wave frequency s, generated with $\mathcal{S}=10$ and different h_0 values, showing the dominating wave families. The circles correspond to the maximal thickness of the waves obtained via transient computations of Eq. (39).

Numerical solutions featuring natural waves were obtained starting from either one of the initial conditions

$$h(x,0) = h_0\{1 + 0.001\,\exp(-10[x-5]^2)\}, \qquad (55)$$

$$h(x,0) = h_0\{0.5[0.05 + \tanh(10[x-5]) + 1]\}, \qquad (56)$$

and subject to $h(0,t)=h_0$, $h_{xxx}(0,t)=0$ and decay conditions downstream from the inlet. The initial conditions in Eqs. (55) and (56) represent an initially flat film subjected to a small-amplitude perturbation and a film with a severely thinned region near the inlet, respectively. The latter could arise in cleaning-type applications wherein an "edge" could develop in a film of material that adheres to an underlying solid substrate which then propagates downstream, leading to the ultimate removal of the layer. For forced waves, solutions are obtained starting from $h(x,0)=h_0$ and the forcing is applied by the following boundary condition:

$$h(0,t) = h_0 + a\cos(\omega t), \qquad (57)$$

where $a \ll h_0$ is the forcing amplitude. Solutions were computed over a wide range of system parameters, $0.05 \leqslant h_0 \leqslant 0.6$, $3 \leqslant \mathcal{S} \leqslant 15$, and $5.26 \leqslant \omega \leqslant 47.6$ with $a=0.04$ on domain lengths of up to 200 dimensionless units using up to 10 000 and 100 000 grid points with EPDCOL and the finite-differences procedure, respectively. In the simulations wherein $h \rightarrow 1$, the computations were halted when spatial derivatives could no longer be resolved accurately.

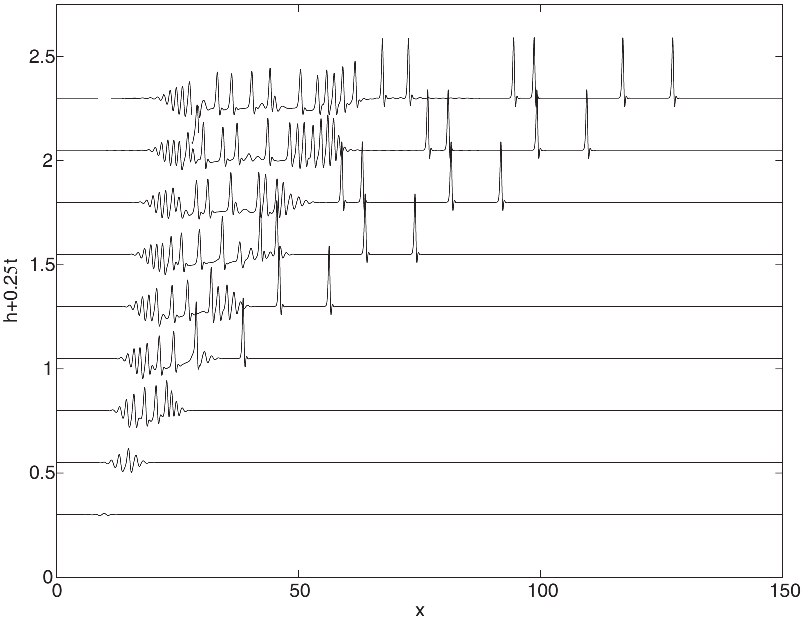

FIG. 4. Space-time plot depicting the film evolution starting from Eq. (55) with $h_0=0.3$ and $S=10$ shown at $t=1.5,2,2.5,3,3.5,4,4.5,5$ (from bottom to top, respectively).

B. Transient-wave formation

1. Natural waves

We begin the presentation of our results by showing in Fig. 4 the film evolution for $h_0=0.3$ and $S=10$ starting from Eq. (55). Inspection of Fig. 4 reveals that disturbances are transported from the vicinity of the inlet to form a wave packet. This is convected away from the inlet and gives rise to large-amplitude waves that interact and coalesce as they propagate rapidly downstream, as shown in Fig. 4. With the exception of a region of approximately uniform thickness near the inlet (this region is actually wavy but the waves are not discernible on the scale used to present Fig. 4) the rest of the interface is populated with pulselike large-amplitude waves; an enlarged view of the region $132 \leqslant x \leqslant 138$ of Fig. 4 is shown in Fig. 5, which depicts such a pulselike solution. The length of the smooth inlet region increases with time as is also shown in Fig. 4. It is also noteworthy that the average film thickness in the wavy region of the film is smaller than that in the smooth region located upstream; this is due to the increase in average velocity in the wavy region. Similar results to those shown in Fig. 4 have also been reported in studies of falling films [57] and thin-film flow over spinning disks [53–56].

In Fig. 6, we show a space-time plot of the film evolution for $h_0=0.3$ and $\mathcal{S}=5$; the lower value of $\mathcal{S}$ used to generate this plot reflects a decrease in the relative significance of inertial forces. It is clearly seen that the degree of interfacial waviness decreases as a result of decreasing $\mathcal{S}$ (note the lower scale of the ordinate in Fig. 6 as compared to that in Fig. 4). Although the disturbance is convected away from the inlet in the form of a wave packet, which is similar to the

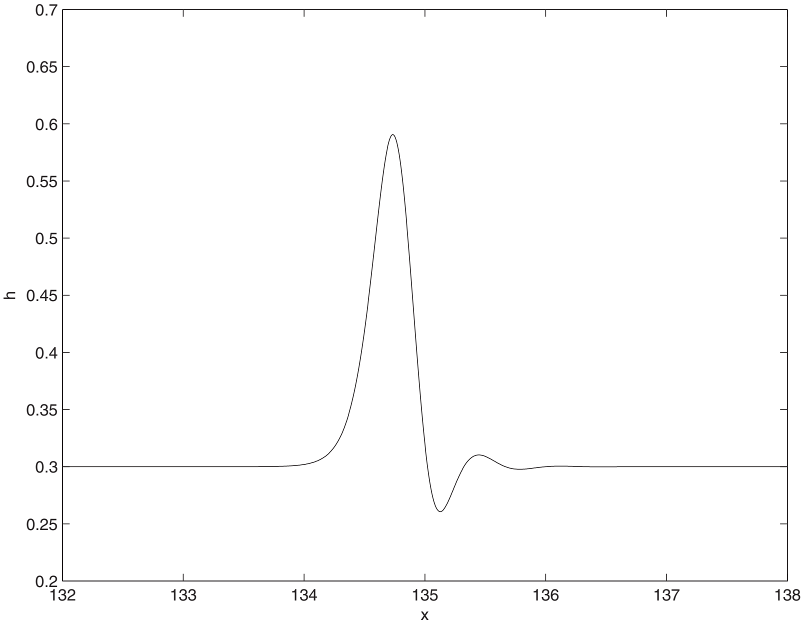

FIG. 5. An enlarged view of the region $132 \leqslant x \leqslant 138$ in Fig. 4 at $t=5$ showing a single large-amplitude pulselike solution.

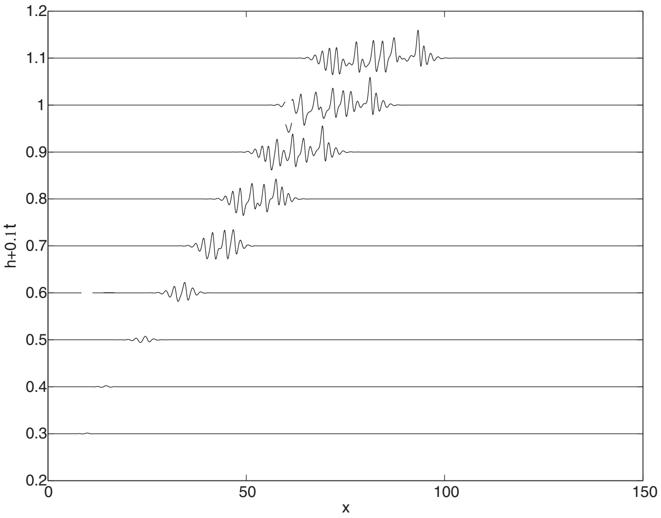

FIG. 6. Space-time plot depicting the film evolution starting from Eq. (55) with $h_0=0.3$ and $\mathcal{S}=5$ shown at $t=1.5,2,3,4,5,6,7,8,9,10$ (from bottom to top, respectively).

dynamics observed for $\mathcal{S}=10$ at early times, large-amplitude pulses are not "radiated" away from this packet, in contrast to the $\mathcal{S}=10$ case. Similar results are obtained by keeping $\mathcal{S}=10$ fixed and decreasing h_0 to $h_0=0.1$. As shown in Fig. 7, the waves that accompany the flow in this case are of small amplitude and do not correspond to coherent structures: these waves propagate as wave packets without radiating pulses and the interfacial dynamics is chaotic and reminiscent of that obtained from the solution of the Kuramoto-Sivashinskiy equation; similar observations were made for falling films at relatively small flow rates [57]. Increasing the value of h_0 to $h_0=0.5$ while keeping $\mathcal{S}=5$ fixed, on the other hand, resulted in wave dynamics that resemble those obtained for $h_0=0.3$ and $\mathcal{S}=10$, as shown in Fig. 8. Thus increasing $\mathcal{S}$ while keeping h_0 fixed or *vice versa* gives rise to similar interfacial dynamics: emergence of coherent structures through coalescence and coarsening of small-amplitude waves, leading to the formation of pulses at relatively high $\mathcal{S}$ and/or h_0, and chaotic dynamics and loss of coherence for relatively small $\mathcal{S}$ and/or h_0.

Our numerical simulations have also shown that an increase in inertial contributions beyond a critical level quickly leads to a channel "bridging" event as the film thickness approaches unity; this results in a singularity which heralds the breakdown of the model. The results shown in Figs. 9 and 10 are typical of the behavior expected of Benney-like equations in the presence of significant inertial forcing [39,58,59]. This behavior is also analogous to the initiation of "slugs" from large waves in pressure-driven gas-liquid flows [26,27]. The pathway to channel bridging is shown in Fig. 9 for $h_0=0.3$ and $\mathcal{S}=12$: large-amplitude waves are quickly established at such large values of $\mathcal{S}$, which coalesce as they propagate downstream, leading to the formation of a wave whose peak approaches the channel upper wall; similar results were obtained by fixing $\mathcal{S}=10$ and increasing h_0 beyond $h_0=0.3$ (not shown)—that is, into the range wherein hysteresislike behavior was observed in Fig. 3. Thus, the onset of this behavior of the traveling-wave solutions can be interepreted as being the precursor of channel bridging. The variation of the time taken for $h\rightarrow 1$, t_b, with h_0 for $\mathcal{S}=10$ was also examined and is depicted in Fig. 10. As shown in this plot, t_b undergoes a catastrophic decrease as h_0 approaches unity. It is important to reiterate that our model will break down when the interface is within a distance of $O(\epsilon^{1/3})$ of the upper wall [37]; thus, the results presented which exhibit bridging should be interpreted with caution. The conditions may indeed be conducive for the formation of large-amplitude waves, and the interface may approach the upper wall; however, our model is unable to capture this stage of the dynamics faithfully due to breakdown of its underlying assumptions.

Next we present a typical film evolution starting from an initial condition described by Eq. (56). This represents a film with a pronounced thinning region near the inlet; this will be

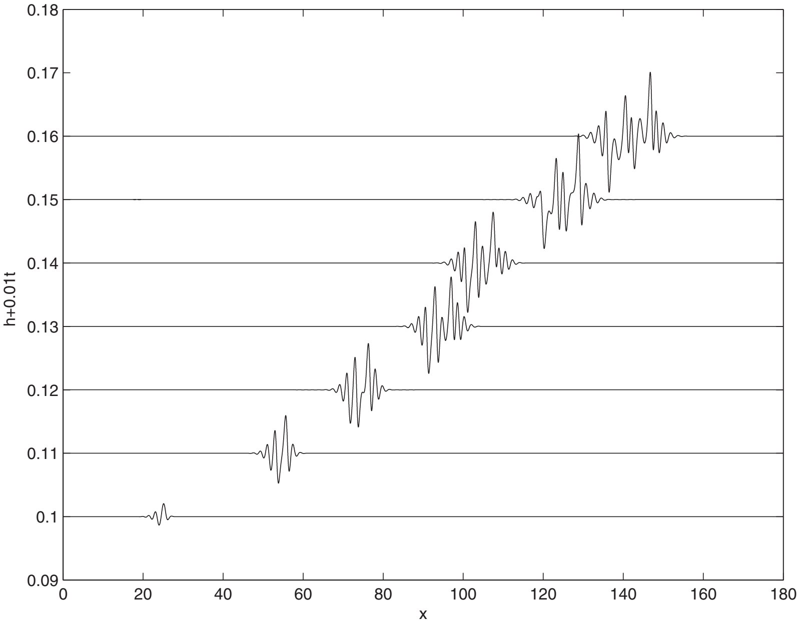

FIG. 7. Space-time plot depicting the film evolution starting from Eq. (55) with $h_0=0.1$ and $\mathcal{S}=10$ shown at $t=20,50,70,90,100,120,137$ (from bottom to top, respectively).

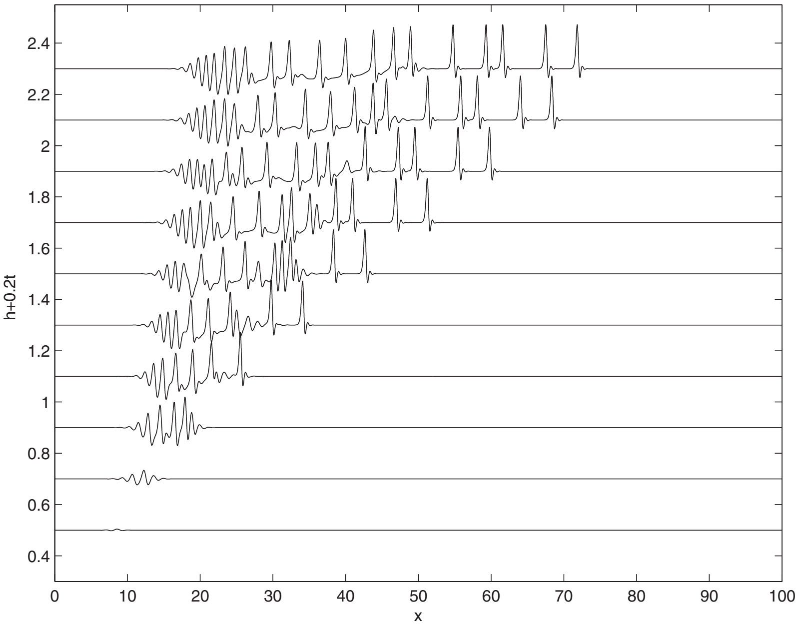

FIG. 8. Space-time plot depicting the film evolution starting from Eq. (55) with $h_0=0.5$ and $S=5$ shown at $t=0.05,0.1,0.15,0.2,0.25,0.3,0.35,0.4,0.45,0.47$ (from bottom to top, respectively).

referred to below as the "edge" of the film. As shown in Fig. 11 at $t=2.8$, the imposed flow in the upper layer drives a flow in the lower layer which causes further thinning of the edge region. This thinning is accompanied by the formation of large-amplitude waves that propagate downstream of the edge and contribute to the reduction of the average thickness of the layer away from the inlet, as shown in Fig. 11 at $t=4.8$ and 8.8. The film continues to thin under the action of the imposed upper layer flow following the propagation of the waves out of the solution domain (see Fig. 11 at $t=24.8$). This flow results in the removal of a very large proportion of the film at late times, as shown in Fig. 11 at $t=198.8$.

2. Forced waves

Finally, we present the results of our simulations of wave formation in the presence of inlet forcing using Eq. (57). An example of the results obtained from such transient computations is shown in Fig. 12. Panel (a) of Fig. 12 depicts a snapshot of the film thickness evolution at $t=5$. It is clearly seen that the presence of forcing gives rise to various regions along the channel axis x, which are populated by different types of wave structures: close to the inlet, $x\in(5,40)$, we observe developed periodic structures; intermediate wave structures are observed at larger values of x $[x\in(40,70)]$, and solitarylike structures are found far from the inlet. The wave structures in the first region are periodic in space as well in time, as demonstrated by panels (b) and (c) wherein the temporal evolution of the film thicknesses, $h(t)$, is presented at two different stations $x_a=7.5$ and $x_b=30$, respectively.

We have compared the results of our transient simulations with the steady traveling-wave solutions obtained via the solution of the nonlinear eigenvalue problem, Eqs. (52)–(54).

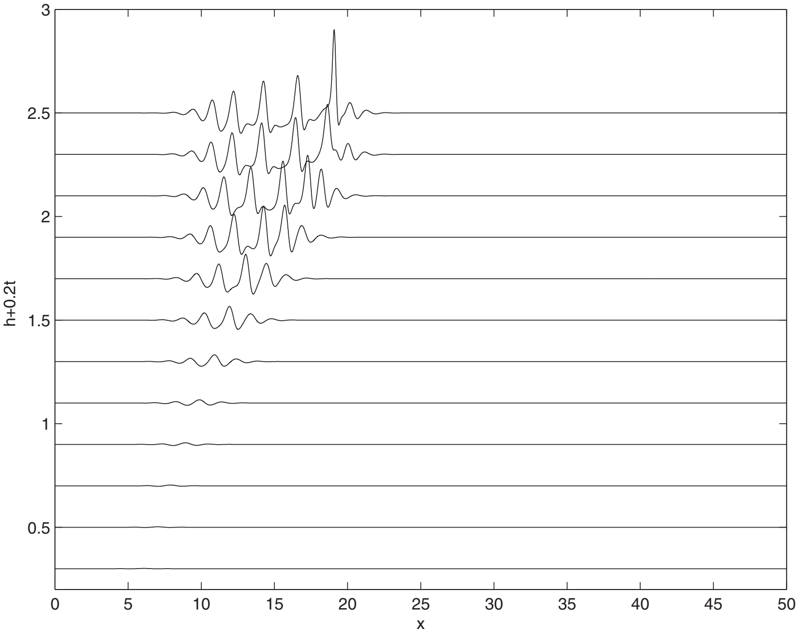

FIG. 9. Space-time plot depicting the film evolution starting from Eq. (55) with $h_0=0.3$ and $S=12$ shown at $t=0.1,0.2,0.3,0.4,0.5,0.6,0.7,0.8,0.9,1,1.06,1.07$ (from bottom to top, respectively).

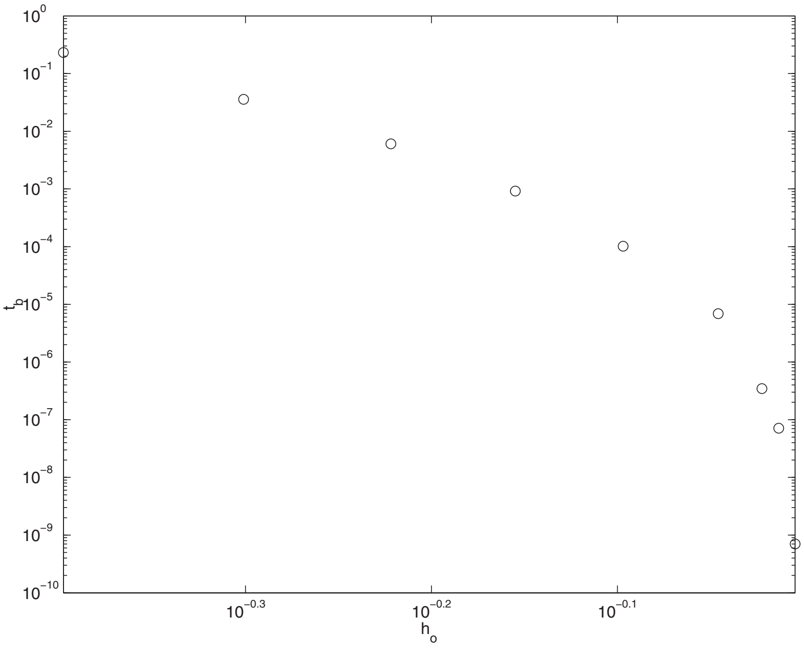

FIG. 10. A log-log plot of the time taken for h to approach unity, t_b, versus the initial film thickness h_0, with $\mathcal{S}=10$.

Panel (d) of Fig. 12 shows a comparison of these solutions at x_a and demonstrates the excellent agreement found. In panel (e) we use the so-called "space delay coordinates" [60] to illustrate the synchronization of the developing wave structures as a result of inlet forcing. We have also determined the maximal film thickness values of the forced waves computed using our transient simulations and compared these with those obtained from Eqs. (52)–(54) as a function of s and given h_0 and $\mathcal{S}$. The circles in Fig. 3 show our simulations results and demonstrate that the waves obtained from the transient computations correspond to "dominating waves," which, in turn, are the steady-traveling waves described in Sec. III B. Other solutions of Eqs. (52)–(54) which may exist do not possess the property of "attraction" and would therefore not be observed in numerical or physical experiments.

V. CONCLUSIONS

We have studied the channel flow of two viscous, immiscible fluids of similar densities in the limit of large viscosity ratios. This situation is representative of one that might arise in cleaning applications wherein a fast-moving layer of one fluid flows past a layer of a much more viscous fluid. We use lubrication theory in the highly viscous layer and a Kármán-Polhausen approximation in the less viscous one to derive a single equation that governs the interfacial dynamics. This equation reduces to a Benney-like equation and the well-studied Kuramoto-Sivashinskiy equation in the appropriate limits. The results of our bifurcation analysis, which is used to compute traveling-wave solutions, demonstrate the existence of solution nonuniqueness in certain regions of param-

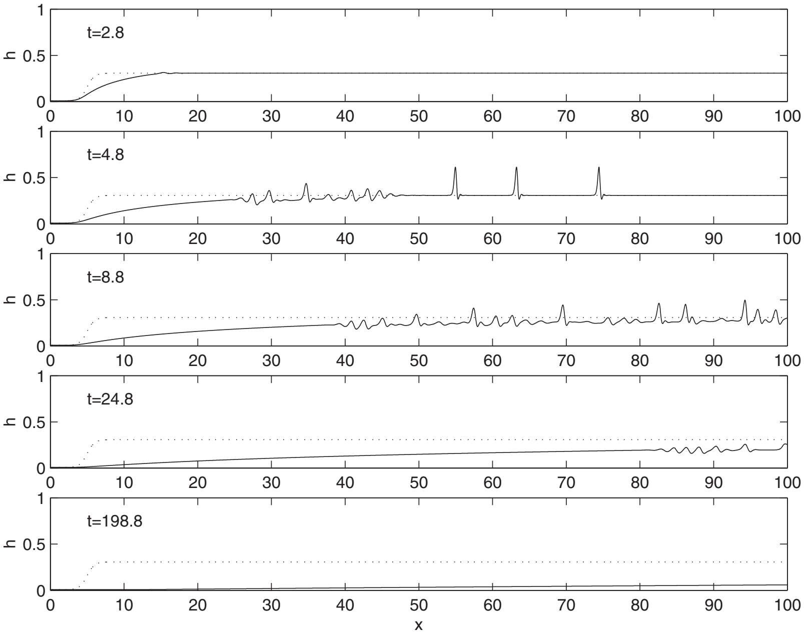

FIG. 11. Numerical solutions for the film evolution (solid lines) starting from Eq. (56), shown as dotted lines, with $h_0=0.3$ and $S=10$ shown at $t=2.8, 4.8, 8.8, 24.8, 198.8$.

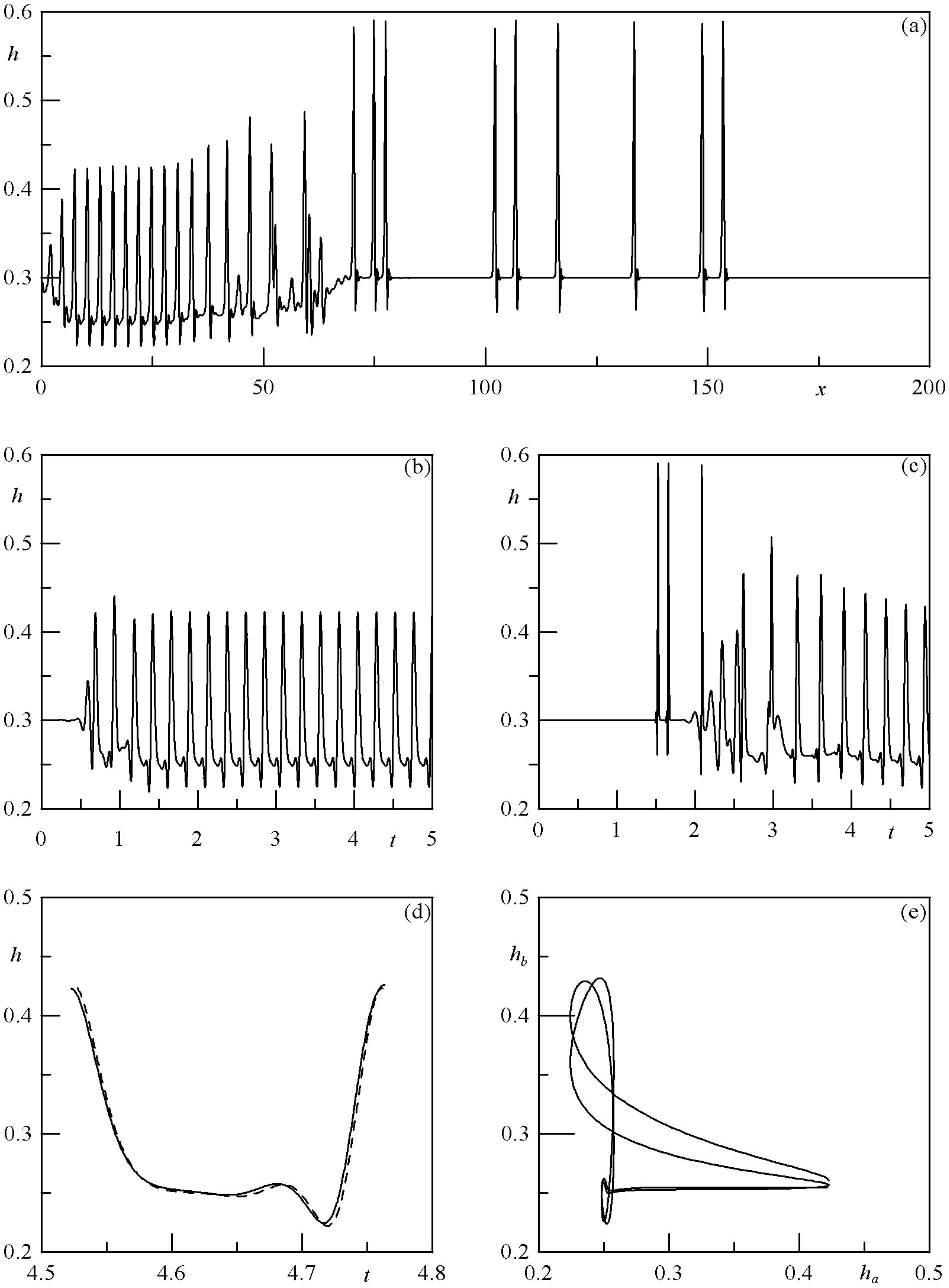

FIG. 12. Transient simulations of wave formation in the presence of inlet forcing starting from $h(x,0)=h_0=0.3$ and using Eq. (57) with $a=0.04$, $s=0.5$, and $\mathcal{S}=10$: (a) spatial development of the film thickness at $t=5$; (b) and (c) temporal evolution of the film thickness at $x_a=7.5$ and $x_b=30$, respectively; (d) comparison of the wave shape $h(t)$ at $x_a=7.5$ (solid curve) and steady-traveling wave (dashed curve), obtained via the solution of Eqs. (52)–(54); (e) dependence of $h_a=h(x_a,t)$ on $h_b=h(x_b,t)$ at $t\in(4,5)$.

eter space. Our transient numerical simulations reveal the formation of large-amplitude waves for significant inertial contributions and/or sufficiently large mean thickness. In the presence of inlet frequency forcing, the transient simulation results are in good agreement with the predictions of the bifurcation analysis.

Future work will focus on situations in which inertia is important in both layers. In this case, a pair of coupled evolution equations for the film thickness and volumetric flow rate of the more viscous layer will be used to study the interfacial dynamics. It would also be of practical interest to examine situations in which the flow in the less viscous layer is turbulent. Here the evolution equations would require closure relations for the interfacial and wall shear stresses. Finally, the flow of two miscible layers in a channel in the absence of a sharp interface and in the presence of non-Newtonian effects would also be of interest. Research in all of these areas is already underway.

ACKNOWLEDGMENTS

We acknowledge support from the Department of Trade and Industry through the “Zero Emission Enterprise—Minimizing the environmental footprint of FMCG plant: Improved cleaning processes” scheme. We also acknowledge fruitful discussions with Professor Burt Tilley, and we are grateful for his careful reading of an earlier version of this paper.

[1] A. Oron, S. H. Davis, and S. G. Bankoff, Rev. Mod. Phys. **69**, 931 (1997).
[2] R. Duenckel (unpublished).
[3] A. E. Dukler, J. A. Fabre, J. B. McQuillen, and R. Vernon, Int. J. Multiphase Flow **14**, 389 (1988).
[4] S. G. Bankoff and S. C. Lee, *Multiphase Science and Technology* (Hemisphere, New York, 1986).
[5] W. S. Bousman, J. B. McQuillen, and L. C. Witte, Int. J. Multiphase Flow **22**, 1035 (1996).
[6] H.-C. Chang, Chem. Eng. Sci. **41**, 2463 (1986).
[7] A. C. Fowler and P. E. Lisseter, SIAM J. Appl. Math. **52**, 15 (1992).
[8] C. Kouris and J. Tsamopoulos, Phys. Fluids **14**, 1011 (2002).
[9] D. Marchesin and B. J. Plohr, SPE J. **6**, 209 (2001).
[10] G. Moritis, Oil & Gas J. **99**, 66 (2001).
[11] K. Pettigrew, J. Kirshberg, K. Yerkes, D. Trebotich, and D. Liepmann (unpublished).
[12] G. Oddie and J. R. A. Pearson, Annu. Rev. Fluid Mech. **36**, 149 (2004).
[13] I. Mudawar, IEEE Trans. Compon. Packag. Technol. **24**, 122 (2001).
[14] W. Qu and I. Mudawar, IEEE Trans. Compon. Packag. Technol. **26**, 598 (2003).
[15] G. F. Hewitt, in *Handbook of Multiphase Systems*, edited by G. Hestroni (Hemisphere, New York, 1982), Chap. 2.
[16] P. Y. Lin and T. J. Hanratty, Int. J. Multiphase Flow **12**, 79 (1986).
[17] N. Andritsos and T. J. Hanratty, Int. J. Multiphase Flow **13**, 444 (1987).
[18] Y. Taitel and A. E. Dukler, AIChE J. **22**, 47 (1976).
[19] C. S. Yih, J. Fluid Mech. **27**, 337 (1967).
[20] E. J. Hinch, J. Fluid Mech. **144**, 463 (1984).
[21] S. G. Yiantsos and B. G. Higgins, Phys. Fluids **31**, 3225 (1988).
[22] R. H. M. Miesen and B. J. Boersma, J. Fluid Mech. **301**, 175 (1995).
[23] W. C. Kuru, M. Sangalli, D. D. Uphold, and M. J. McReady, Int. J. Multiphase Flow **21**, 733 (1995).
[24] P. A. M. Boomkamp and R. H. M. Miesen, Int. J. Multiphase Flow **22**, 67 (1996).
[25] T. Boeck and S. Zaleski, Phys. Fluids **17**, 032106 (2005).
[26] R. I. Issa and M. H. W. Kemp, Int. J. Multiphase Flow **29**, 69 (2003).
[27] M. Bonizzi and R. I. Issa, Int. J. Multiphase Flow **29**, 1719 (2003).
[28] J. Li and Y. Y. Renardy, J. Fluid Mech. **391**, 123 (1999).
[29] W. Tauber and S. O. Unverdi, Phys. Fluids **14**, 2871 (2002).
[30] T. Boeck, J. Li, E. Y. E. Lopez-Pages, and S. Zaleski, Theor. Comput. Fluid Dyn. **21**, 59 (2007).
[31] P. Valluri, P. D. M. Spelt, C. J. Lawrence, and G. F. Hewitt (unpublished).
[32] D. S. Loewenherz and C. J. Lawrence, Phys. Fluids A **1**, 1686 (1989).
[33] I. L. Kliakhandler, J. Fluid Mech. **391**, 45 (1999).
[34] B. S. Tilley, S. H. Davis, and S. G. Bankoff, J. Fluid Mech. **277**, 55 (1994).
[35] B. S. Tilley, S. H. Davis, and S. G. Bankoff, Phys. Fluids **6**, 3906 (1994).
[36] D. T. Papageorgiou, C. Maldarelli, and D. S. Rumschitzki, Phys. Fluids A **2**, 340 (1990).
[37] T. Segin, B. S. Tiley, and L. Kondic, J. Fluid Mech. **532**, 217 (2005).
[38] T. Segin, B. S. Tiley, and L. Kondic, IMA J. Appl. Math. **71**, 715 (2006).
[39] D. J. Benney, J. Math. Phys. **45**, 150 (1966).
[40] C. Ruyer-Quill and P. Manneville, Eur. Phys. J. B **15**, 357 (2000).
[41] C. Ruyer-Quil and P. Manneville, Phys. Fluids **14**, 170 (2002).
[42] B. Scheid, C. Ruyer-Quil, U. Thiele, O. A. Kabov, J. C. Legros, and P. Collinet, J. Fluid Mech. **527**, 303 (2005).
[43] B. Scheid, C. Ruyer-Quil, S. Kalliadasis, M. G. Velarde, and R. K. Zeytounian, J. Fluid Mech. **538**, 199 (2005).
[44] B. Scheid, C. Ruyer-Quil, S. Kalliadasis, M. G. Velarde, and R. K. Zeytounian, J. Fluid Mech. **538**, 223 (2005).
[45] G. M. Homsy, Lect. Appl. Math. **15**, 191 (1974).
[46] Y. Kuramoto and T. Tsuzuki, Prog. Theor. Phys. **55**, 356 (1976).
[47] G. I. Sivashinsky, Acta Astron. **4**, 1177 (1977).
[48] D. Gotlieb and S. A. Orszag, *Numerical Analysis of Spectral Methods: Theory and Applications* (SIAM, New York, 1977).
[49] G. M. Sisoev, O. K. Matar, R. V. Craster, and S. V. Gerasimov, Chem. Eng. Sci. **61**, 7279 (2006).
[50] G. M. Sisoev and V. Y. Shkadov, Phys. Dokl. **42**, 683 (1997).
[51] V. Y. Shkadov and G. M. Sisoev, Comput. Fluids **34**, 151 (2005).
[52] P. Keast and P. H. Muir, ACM Trans. Math. Softw. **17**, 153 (1991).
[53] O. K. Matar, G. M. Sisoev, and C. J. Lawrence, Phys. Fluids **16**, 1532 (2004).
[54] O. K. Matar, G. M. Sisoev, and C. J. Lawrence, Phys. Fluids **17**, 052102 (2005).
[55] O. K. Matar and C. J. Lawrence, Chem. Eng. Sci. **61**, 1074 (2006).
[56] O. K. Matar and C. J. Lawrence, Chem. Eng. Sci. **61**, 3838 (2006).
[57] H.-C. Chang and E. Demekhin, *Complex Wave Dynamics on Thin Films* (Elsevier, Amsterdam, 2002).
[58] S. Kalliadasis and C.-H. Chang, J. Fluid Mech. **261**, 135 (1994).
[59] V. I. Kerchman and A. L. Frenkel, Theor. Comput. Fluid Dyn. **6**, 234 (1994).
[60] J. Liu and J. P. Gollub, Phys. Fluids **6**, 1702 (1994).